PHOTONICS Research

On-chip ultra-high rejection and narrow bandwidth filter based on coherency-broken cascaded cladding-modulated gratings

Jinzhao Wang,[1] Ting Li,[2] Yang Feng,[1] Jiewen Li,[1] Wanxin Li,[1] Luwei Ding,[1] Yong Yao,[1] Jianan Duan,[1] Wei Liu,[1] Feng He,[1] Yi Zou,[2,3] and Xiaochuan Xu[1,*]

[1]Guangdong Provincial Key Laboratory of Integrated Photonic-Electronic Chip, Guangdong Provincial Key Laboratory of Aerospace Communication and Networking Technology, Harbin Institute of Technology, Shenzhen, Shenzhen 518055, China
[2]School of Information Science and Technology, ShanghaiTech University, Shanghai 201210, China
[3]e-mail: zouyi@shanghaitech.edu.cn
*Corresponding author: xuxiaochuan@hit.edu.cn

Received 3 November 2023; revised 22 February 2024; accepted 8 March 2024; posted 11 March 2024 (Doc. ID 510899); published 1 May 2024

Bragg filters are of essential importance for chip-scale photonic systems. However, the implementation of filters with sub-nanometer bandwidth and rejection beyond 70 dB is hindered by the high index contrast of the silicon-on-insulator platform, which makes filters prone to fabrication imperfections. In this paper, we propose to combine coherency-broken cascading architecture and cladding modulation to circumvent the intrinsic limitation. The cascading architecture effectively prevents the accumulation of phase errors, while the cladding modulation offers additional design freedom to reduce the coupling coefficient. A bimodal Bragg filter with a testing-equipment-limited rejection level of 74 dB and a 40 dB bandwidth of 0.44 nm is experimentally demonstrated. The minimum feature size is 90 nm, which significantly relieves the fabrication constraints.

https://doi.org/10.1364/PRJ.510899

1. INTRODUCTION

The rapid development of silicon photonics has stimulated broad interest in chip-scale photonic systems, such as on-chip signal processing [1,2], microwave photonics [3], and integrated quantum photonics [4,5]. As one of the fundamental building blocks, on-chip filters, including Bragg grating filters [4,6–8], micro-resonators [9–11], Mach–Zehnder interferometers (MZIs) [12,13], and contra-directional couplers [14–16], play a vital role in the performance of these systems. Among these filter structures, Bragg gratings have been widely used on many platforms for decades. Bragg grating filters couple optical signals near the Bragg wavelength into the backward-propagating mode, enabling a band-stop filter at the through port and a band-pass filter at the reflection port [17]. As a classic filter structure, the Bragg grating has a few distinct features, such as wide free spectral range (FSR) and low insertion loss [11,15,18], making it an appealing candidate for on-chip spectrum management.

However, achieving high rejection and narrow bandwidth simultaneously on silicon-on-insulator (SOI) is challenging due to the high index contrast. Based on the coupled mode theory, the rejection (R) and transmission spectrum bandwidth ($\Delta\lambda$) of an ideal uniform Bragg grating filter are related to the coupling coefficient (κ) and filter length (L_F) by [19]

$$R = \tanh^2(\kappa L_F), \tag{1}$$

$$\Delta\lambda = \frac{\lambda_0^2}{\pi n_g}\sqrt{\kappa^2 + \frac{\pi^2}{L_F^2}}, \tag{2}$$

where n_g is the group index of the propagation mode. According to Eqs. (1) and (2), any rejection and spectrum bandwidth could be readily realized by selecting a proper combination of κ and L_F. However, due to the accumulation of phase errors induced by fabrication imperfections, such as side-wall roughness [20], the experimentally demonstrated rejection of conventional single-section Bragg filters hardly exceeded 45 dB on the SOI platform [4,21,22]. The limited rejection strength hinders the development of on-chip nonlinear photonic systems such as integrated quantum photonics [23–25]. For instance, on-chip photon pair generation based on spontaneous four-wave mixing (SFWM), which usually involves a strong pump injection ratio [26], requires more than 100 dB rejection and narrow bandwidth for effective noise

suppression and signal extraction [27–29]. As a result, additional filters, either off-chip or on another chip, have to be used.

Besides, Eq. (2) suggests that to realize sub-nanometer bandwidth filters, the structural modulation of a conventional on-chip Bragg grating has to be within a few nanometers [30]. Recent research shows that the sidewall roughness is around a couple of nanometers (1.8 nm in Ref. [30] and 2.7 nm in Ref. [31]). It has been proven that such roughness can significantly distort the spectral response of Bragg gratings, especially long gratings [32]. It means that the dimension of the structure is in the same order as the sidewall roughness. Apparently, the required fabrication precision is far beyond the capability of currently commercialized silicon photonics foundries.

In this paper, we apply the coherency-broken configuration for cascaded cladding-modulated bimodal waveguide Bragg gratings to break the intrinsic limits on rejection and spectrum bandwidth. The coherency-broken cascade configuration mitigates the accumulation of phase errors, thus effectively suppressing the impact of fabrication imperfections on the rejection level. The narrow bandwidth is realized by employing the cladding-modulated grating structure, which significantly increases minimum feature sizes to tens of nanometers by avoiding directly modulating the waveguide [33–35]. This generic strategy paves the way towards on-chip integration of advanced nonlinear photonic systems.

2. WORKING PRINCIPLE

The schematic of the proposed coherency-broken cascaded cladding-modulated grating filter is illustrated in Fig. 1(a). A bimodal grating is leveraged to separate the forward- and backward-propagating optical waves into TE_0 and TE_1 modes,

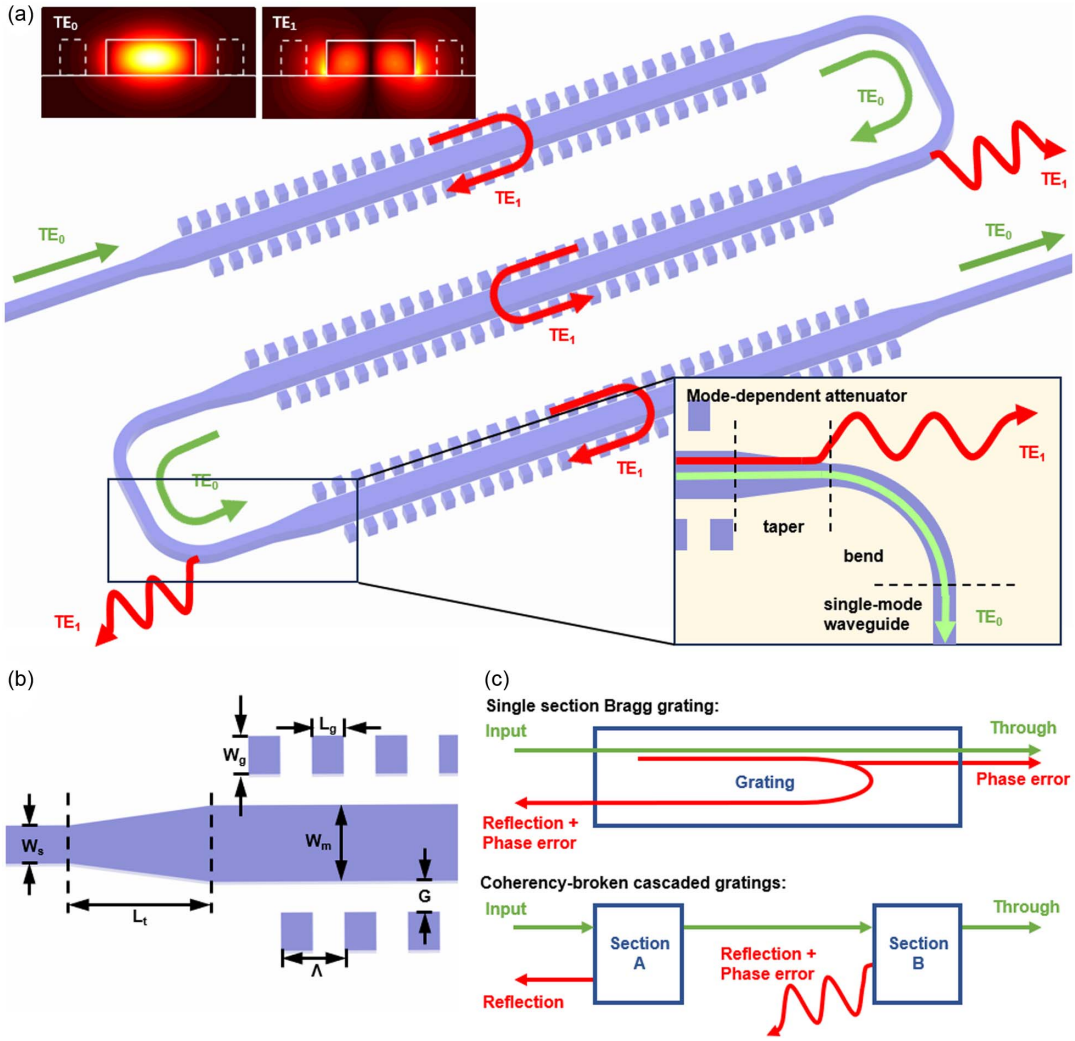

Fig. 1. (a) Schematic of the proposed coherency-broken cascaded cladding-modulated Bragg grating filter. The incident fundamental mode (TE_0) converts into the backward-propagating first-order mode (TE_1) as it passes through each section of the grating. The adjacent sections of the grating are mode-dependent attenuators composed of tapers, single-mode waveguides, and bends, which efficiently radiate and dissipate the backward-propagating TE_1 mode. Top left: electric field intensity distribution of TE_0 and TE_1 modes of the bimodal waveguide. Bottom right: schematic representation of the propagation characteristics of TE_0 and TE_1 modes in the mode-dependent attenuator. TE_1 mode experiences significantly higher propagation loss than TE_0 mode. (b) Schematic of the asymmetric Bragg grating geometry. (c) Diagram illustrating the effect of phase error on the grating operation of single-section Bragg grating and coherency-broken cascaded gratings.

respectively. The filter comprises N bimodal grating sections connected with mode-dependent attenuators. The structure of the asymmetric bimodal phase-shifted Bragg grating is shown in Fig. 1(b). Instead of directly modulating the waveguide core, e.g., sidewall corrugation, a cladding-modulated grating is formed by a periodic array of silicon blocks on both sides of the bimodal waveguide. As shown by the top left inset of Fig. 1(a), the blocks interact with the evanescent field of the guided modes. This configuration provides additional degrees of design freedom in tailoring the grating coupling coefficient κ. By adjusting the gap G between silicon blocks and the central waveguide, a sufficiently small coupling coefficient can be generated with fabrication-friendly critical dimensions [36]. The period Λ of the bimodal waveguide Bragg grating can be calculated by the classic phase matching condition $\lambda_0 = \Lambda(n_{\text{eff}1} + n_{\text{eff}2})$, where $n_{\text{eff}1}$ and $n_{\text{eff}2}$ are the effective indices of the TE_0 and TE_1 modes of the bimodal waveguide, respectively. The silicon blocks on one side of the grating are shifted by half a period to assist the conversion of the forward-propagating TE_0 mode to the backward-propagating TE_1 mode [4]. As illustrated in Fig. 1(c), the single-section Bragg grating reflects light back into the input waveguide through constructive interference of partial reflections occurring in each period at Bragg wavelength. According to Eq. (1), for single-section grating filters, the rejection primarily depends on the grating-assisted coupling strength between the TE_0 and the TE_1 mode and the length of the grating. In the experiment, the presence of phase errors destroys the perfect coherent interference, leading to the forward-propagating photons in the stop-band and consequently compromising the rejection strength, as illustrated by the red lines in Fig. 1(c). Since the phase error accumulates with grating length, improving the rejection strength by increasing grating length becomes ineffective. Directly connecting multiple sections of filters also cannot avoid the accumulation of phase errors [37]. In the meantime, the phase errors distort the spectral response, resulting in the bandwidth broadening of the cascaded filter. Thus, even in the presence of negligible fabrication imperfections in the grating, the relative phase shift between two cascaded gratings still needs to be tightly controlled.

To overcome this limitation, it is of crucial importance to prevent the accumulation of phase errors. Thus, instead of directly connecting filters, mode-dependent attenuators are introduced in between filter sections to "drain" photons in the reflection band, as shown in Fig. 1(c). The mode-dependent attenuators can be built readily with bimodal-to-single-mode tapers and single-mode waveguide bend. In these waveguide structures, TE_1 mode experiences significantly higher propagation loss than TE_0 mode [as shown in the inset of Fig. 1(a)], thereby substantially attenuating the coherent interactions between adjacent grating sections and suppressing the accumulation of phase errors.

3. RESULTS

The proposed cladding-modulated Bragg filters are designed and fabricated on SOI with a 220-nm-thick single-crystal silicon device layer and a 2-μm-thick buried oxide (BOX) layer. Electron beam lithography (NanoBeam nB5) with diluted ZEP520A is leveraged for quick prototyping, while the critical dimension of the proposed filter is compatible with the multi-project wafer (MPW) in silicon photonics foundries. Then the designs are transferred into the single-crystal device layer by inductively coupled plasma (ICP) etching. Figure 2(a) shows the optical micrograph of a fabricated filter consisting of seven identical coherency-broken cascaded grating sections. The width of the single-mode waveguide W_s is 450 nm to ensure low propagation loss transmission of the TE_0 mode and the suppression of the TE_1 mode. The width of the bimodal waveguide W_m is 680 nm. The dimensions of silicon blocks are $W_g \times L_g = 200\ \text{nm} \times 175\ \text{nm}$. The period of the grating $\Lambda = 350$ nm is chosen to satisfy the Bragg condition at $\lambda_0 = 1550$ nm. The block array on one side of the grating is shifted by half a period (175 nm) relative to the other side [38]. Each section of the asymmetric bimodal grating has a taper with a length of $L_t = 25$ μm at both ends to achieve the adiabatic conversion of the TE_0 mode from a single-mode waveguide to a bimodal waveguide and vice versa. Between every two grating sections, there is a 130-μm-long straight single-mode waveguide and two single-mode bends with a radius of 10 μm. These structures constitute the mode-dependent attenuator, enabling the radiation of TE_1 mode. According to the simulation, the radiation ratio of TE_1 mode when passing through the taper and a single-mode waveguide can reach at least 15 dB, ensuring the attenuation of phase errors caused by the subsequent filter. Figures 2(b) and 2(c) are the scanning electron microscopy (SEM) images of the single-mode waveguide bend and asymmetric bimodal grating, respectively.

The filters are characterized by a C-band narrow linewidth tunable laser (Santec TSL-550, with a linewidth of 400 kHz) and a power meter (Santec MPM-210). The minimum detectable power of the power meter is approximately −80 dBm, which determines the maximum rejection strength that could

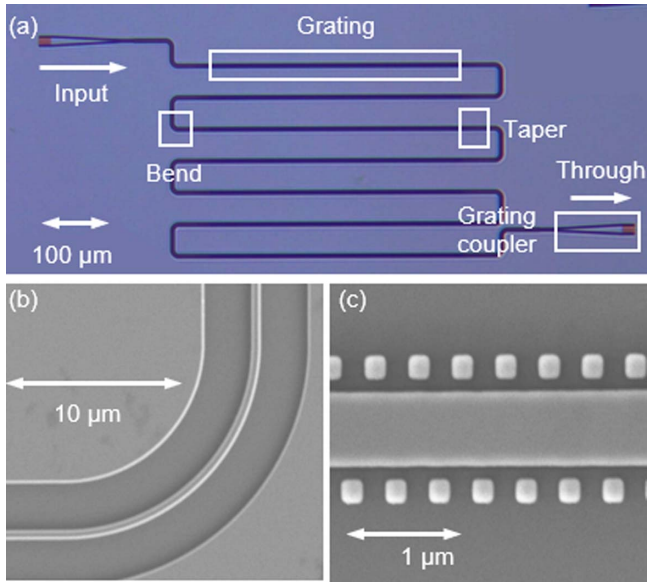

Fig. 2. (a) Microscope image of one of the fabricated coherency-broken cascaded grating filters comprising seven Bragg grating filters. Scanning electron microscope image of (b) single-mode waveguide bend and (c) cladding-modulated grating filter.

be measured with the experiment setup. A polarization-maintaining fixture is employed to ensure the input light is with the transverse-electric (TE) polarization. To demonstrate the coupling strength tuning capability of cladding modulation, the transmission spectra of single-section bimodal Bragg grating filters with three different gaps $G = 80$, 90, and 110 nm are collected and shown in Fig. 3(a). Each filter includes 1700 periods, corresponding to a total length of around 600 μm. For clarity of discussion, the rejection of a filter is defined as the ratio of the off-band transmission to the minimum inside the stop-band. As shown in Fig. 3(a), the rejection strength decreases from 37 to 27 dB as the gap G increases from 80 to 110 nm. The null-to-null bandwidths are 2.06, 1.89, and 1.62 nm for $G = 80$, 90, and 110 nm, respectively. These results, together with our previous demonstration of ultra-long grating antennas [35], have shown that evanescent field modulation is a powerful tool in tailoring the spectral response of gratings.

Figure 3(b) shows the rejection in relation to grating length for a fixed gap $G = 90$ nm. The grating length varies from 400 to 2000 μm. As shown by the red solid line in Fig. 3(b), the rejection of the grating filter with air cladding increases quickly with the grating length. When the grating length reaches 1000 μm, the growth rate starts to decrease. When the filter length exceeds 1500 μm, the rejection saturates at around 45 dB, as indicated by the red dashed line in Fig. 3(b). It indicates that the maximum rejection strength is ultimately limited by the fabrication quality. The high-refractive-index contrast between silicon and air exacerbates the deleterious effects of fabrication imperfections. Intuitively, the phase errors can be reduced by decreasing the index contrast. Thus, a 1.8-μm-thick layer of SU-8 is spin-coated on the chip, reducing the index contrast from 2.47 to 1.89. In the meantime, due to the reduced index contrast, the evanescent wave extends further into the cladding, resulting in the increase of coupling coefficient κ. The rejection of single-section gratings with a gap width of 100 nm and grating lengths varying from 200 to 2000 μm is shown by the blue solid line in Fig. 3(b). It is evident that the SU-8-coated grating filters exhibit significantly higher rejection compared to air-clad gratings when the grating length is relatively short. The rejection approaches saturation when the grating length reaches 600 μm. Even when the grating length increases to 2000 μm, the rejection of a single-section grating filter remains around 50 dB without significant increase. The saturation value is indicated by the blue dashed line in Fig. 3(b). The experimental results have proven the previous discussion that the fabrication sets the upper limit of the rejection strength. Furthermore, when SU-8 cladding is introduced, the stop-band shifts towards longer wavelengths (~30 nm) compared to the filter with air cladding.

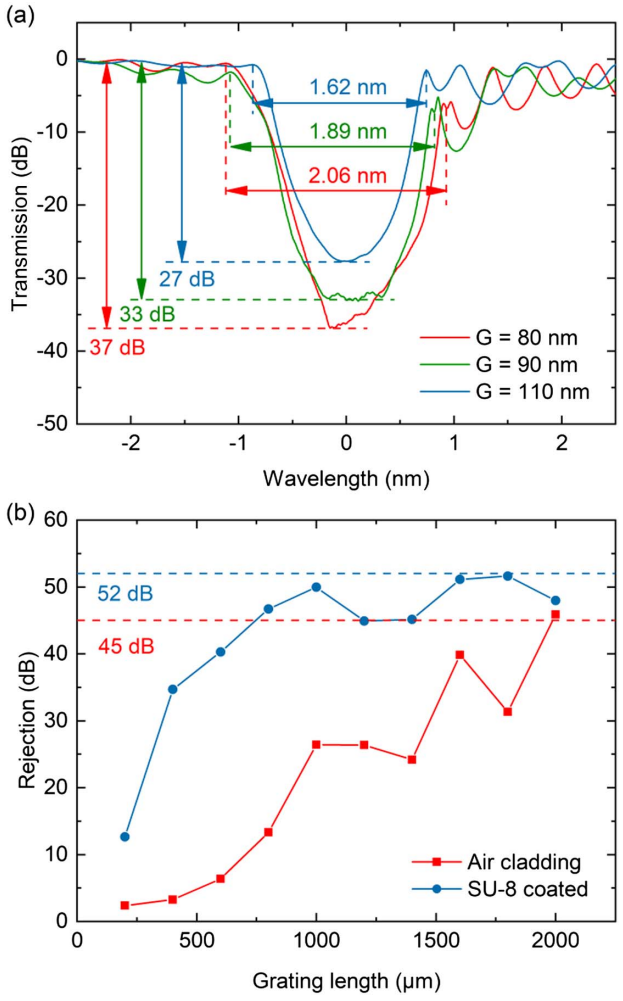

Fig. 3. Measured transmission spectra of single-section Bragg filter with (a) different gap widths ranging from 80 to 110 nm, and (b) single-section filters with different grating lengths ranging from 400 to 2000 μm while gap G equals 90 nm. The red solid line in (b) indicates the rejection of the air cladding grating, and the blue solid line indicates the grating covered by SU-8.

To demonstrate the effectiveness of the coherency-broken cascading architecture in minimizing the impact of phase errors, artificial fabrication errors are introduced into a single-section filter with a length of 2000 μm. For comparison, the transmission spectrum of the filter without artificial defects is shown in Fig. 4(a). The maximum rejection reaches 46 dB. The 3, 20, and 40 dB bandwidths are 1.13, 0.55, and 0.29 nm, respectively. These results are competitive with state-of-the-art single-section grating filters. The defects are created by randomly selecting several silicon blocks and changing their L_g (reduced to random lengths such as 120, 130, or 140 nm), as shown in the inset of Fig. 4(b). Due to the phase errors induced by the artificial defects, the filter exhibits entirely different transmission characteristics. As shown in Fig. 4(b), typical features in the spectral response of Bragg gratings disappear due to the accumulation of phase errors. In Fig. 4(c), the single-section 2000-μm-long grating with the same artificial fabrication errors is divided into two 1000-μm-long sections connected with a mode-dependent attenuator. The transmission spectrum shows that a significant stop-band appears in the spectrum with a rejection strength of 44 dB. The results show that the utilization of the coherency-broken cascade structure can substantially ameliorate the impact of phase errors and improve the spectral response.

To find the number of sections yielding the maximum rejection strength, we divide the 2000-μm-long filter with a gap width of 90 nm into 4, 8, 16, and 20 sections with equivalent length. The measured spectra are shown in Fig. 5(a). It can be

observed that the distortion in the transmission spectrum of the single-section 2000 μm grating is prominent compared to the spectrum shown in Fig. 4(a), indicating the fabrication error varies from chip to chip. Therefore, to systematically study the impact of the number of sections on the rejection level, filters fabricated side-by-side on the same chip are measured. As proved in Fig. 5(a) once again, the coherency-broken cascading effectively suppresses the accumulation of phase errors. The blue plot in Fig. 5(a) (right and top axes) summarizes the measured rejection of filters with different numbers of sections while the total grating length is kept at 2000 μm. It can be observed that there exists the optimal number of sections that maximizes the rejection. Additionally, the filter bandwidth increases as the length of single grating sections decreases, and even the total length of the filter remains the same. This is because the spectral bandwidth is primarily determined by the bandwidth of the single grating sections rather than the total filter length [39].

The comparison of experimentally measured rejection for the single-section and coherency-broken cascaded grating filters is shown in Fig. 5(b). Both sets of filters are fabricated on the same chip and have the same gap $G = 90$ nm. The rejection of the single-section grating filters saturates when the grating length reaches ~1600 μm, as indicated by the red dashed line. This phenomenon accompanied by the spectral disturbance has been observed frequently in our in-house fabricated single-section

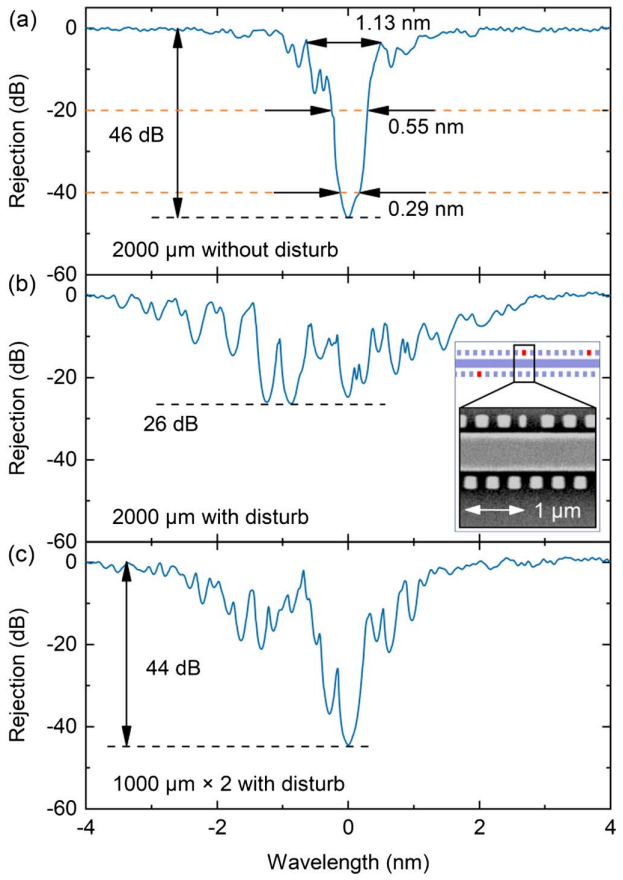

Fig. 4. Measured transmission spectra of (a) single-section 2000-μm-long Bragg filter without artificial imperfections, (b) single-section 2000-μm-long Bragg filters with artificial imperfections, and (c) two sections of cascaded 1000-μm-long Bragg filters with artificial imperfections. The insets of (b) show the grating structure in three different cases, where the introduced imperfections are denoted by red dots.

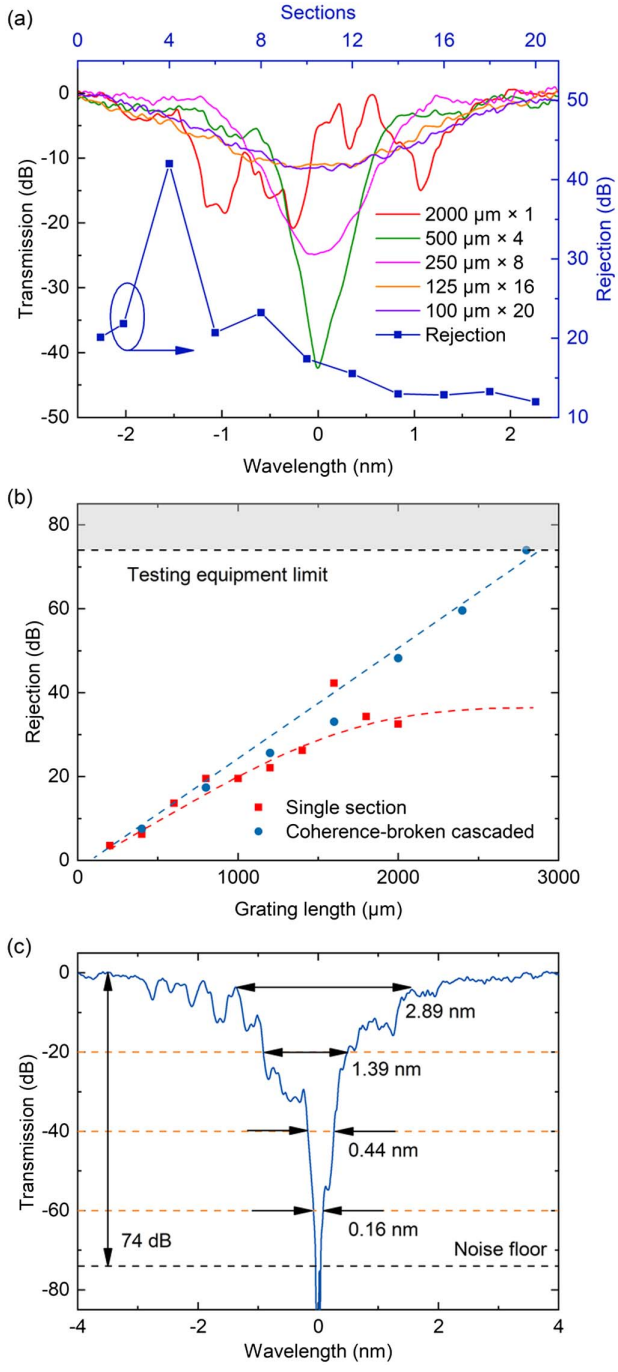

Fig. 5. (a) Measured transmission spectra of 2000 μm × 1, 500 μm × 4, 250 μm × 8, 125 μm × 16, and 100 μm × 20 gratings (left and bottom axes). The blue plot (right and top axes) summarizes the change of the rejection as the number of sections increases. The total grating length is fixed at 2000 μm. (b) Comparison of the rejection of single-section (red square) and coherency-broken cascaded (blue circle) strategy as a function of the filter length. (c) Measured transmission spectrum of the coherency-broken cascaded filter consisting of seven 400 μm Bragg grating sections.

Table 1. Recent Results of On-Chip Silicon Filters Based on Bragg Gratings

Filter Structure		Rejection (dB)	Bandwidth (nm)	Length (μm)
Single-section	Sidewall corrugated grating [38]	34	6 (FWHM)	162
	Curved cladding-modulated grating [40]	23	1.7 (fit)	920
	Spiral sidewall corrugated grating in 60-nm-thick SOI [41]	43	0.94 (FWHM)	2000
	Single-side sidewall corrugated grating [42]	63	18 (40 dB)	450
	Side and top grating [43]	60	7 (40 dB)	670
	Cladding modulated grating (this work)	46	0.29 (40 dB)	2000
Coherency-broken cascading	Sidewall corrugated grating [39]	80	6 (40 dB)	2500
	Sidewall corrugated subwavelength grating [44]	60	3.3 (null-to-null)	2700
	Cladding-modulated grating (this work)	74	0.44 (40 dB)	2800

filters. The rejection of the coherency-broken cascaded filters with total length varying from 400 to 2800 μm is shown by the blue dots in Fig. 5(b). Each of these coherency-broken cascaded filters consists of a different number of grating sections with a length of 400 μm, as illustrated in Fig. 2(a). The experimental results demonstrate that the coherency-broken cascading approach is effective in making the rejection improve with total grating length. The rejection reaches at least 74 dB when the total grating length is 2800 μm and has surpassed the maximum value that can be measured by the testing setup, as indicated by the gray region in Fig. 5(b).

Figure 5(c) shows the transmission spectrum of the filter with a total length of 2800 μm and consisting of seven 400 μm bimodal Bragg grating sections. The rejection of the cascaded filter reaches 74 dB, which is limited by our measurement setup. The filter also has narrow bandwidths of 2.89, 1.39, 0.44, and 0.16 nm when the rejection reaches about 3, 20, 40, and 60 dB, respectively. The rejection band of the output spectrum is located at the noise floor of the power meter (−80 dBm). This result is close to, to the best of our knowledge, the largest rejection experimentally demonstrated for the silicon Bragg grating filters (80 dB). However, due to the utilization of cladding-modulated gratings, our filter exhibits a significantly narrower rejection bandwidth compared to that work (∼10 nm) [39].

Table 1 summarizes the Bragg grating filters reported in recent years. The strip waveguide sidewall corrugation design reaches 34 dB rejection with a 3 dB bandwidth of 6 nm, but the corrugation is only a few nanometers [38]. The filter using a cladding-modulated grating structure can achieve a bandwidth as narrow as 1.7 nm (with a rejection of 23 dB) owing to the reduced coupling coefficient [40]. An alternative to reducing the coupling coefficient is using a thin waveguide core. For instance, Bragg gratings on 60-nm-thick silicon strip waveguides can achieve a narrow bandwidth of 0.94 nm (with a rejection of 43 dB). Compared to the typical 220-nm-thick strip waveguide, the thin waveguide supports a fundamental mode with much lower optical confinement in the waveguide core [41]. Overall, cascaded gratings exhibit significantly higher rejection. The highest rejection achieved so far is approximately 80 dB (6 nm bandwidth) by coherency-broken cascaded 10 Bragg gratings, each with a length of 250 μm [39]. Filters based on Bragg grating geometry have the advantages of subwavelength engineering and coherency-broken cascading to implement narrow bandwidths (3.3 nm) with high rejection levels (60 dB) [44]. In this work, we realize high rejection and narrow bandwidth filters by introducing the coherency-broken cascaded cladding-modulated grating. The present silicon photonic filter has a narrow 40 dB bandwidth of ≈0.44 nm and a high rejection of 74 dB, which is better than most silicon filters based on gratings. Besides, the present silicon photonic filter has a large feature of 90 nm.

4. CONCLUSION

In summary, we exploit a coherency-broken cascade configuration and cladding-modulated bimodal waveguide Bragg gratings to break the intrinsic limits on rejection and spectrum bandwidth. The coherency-broken configuration effectively suppresses the accumulation of phase errors, thereby significantly improving the rejection. By employing the cladding-modulated grating structure, small coupling coefficients can be achieved with a large gap width, which is compatible with photolithography. This research also demonstrates that cladding modulation is an effective approach to break the design constraints of high-index-contrast waveguides, which can give rise to a new category of on-chip devices, such as filters [21,45], sensing [46,47], and antennas [35,48].

Funding. Basic and Applied Basic Research Foundation of Guangdong Province (2020B1515130006, 2021B515120056, 2023A1515011944); Science, Technology and Innovation Commission of Shenzhen Municipality (JCYJ20210324131614040, JCYJ20220531095604009); National Natural Science Foundation of China (U22A2093).

Acknowledgment. The authors thank the ShanghaiTech University Quantum Device Lab (SQDL) for the technical support.

Disclosures. The authors declare no conflicts of interest.

Data Availability. Data underlying the results presented in this paper are not publicly available at this time but may be obtained from the authors upon reasonable request.

REFERENCES

1. M. H. Khan, H. Shen, Y. Xuan, *et al.*, "Ultrabroad-bandwidth arbitrary radiofrequency waveform generation with a silicon photonic chip-based spectral shaper," Nat. Photonics **4**, 117–122 (2010).
2. A. Khilo, S. J. Spector, M. E. Grein, *et al.*, "Photonic ADC: overcoming the bottleneck of electronic jitter," Opt. Express **20**, 4454–4469 (2012).

3. L. Gao, X. Chen, and J. Yao, "Tunable microwave photonic filter with a narrow and flat-top passband," IEEE Microw. Wireless Compon. Lett. **23**, 362–364 (2013).
4. H. Qiu, J. Jiang, P. Yu, *et al.*, "Silicon band-rejection and band-pass filter based on asymmetric Bragg sidewall gratings in a multimode waveguide," Opt. Lett. **41**, 2450–2453 (2016).
5. F. Mazeas, M. Traetta, M. Bentivegna, *et al.*, "High-quality photonic entanglement for wavelength-multiplexed quantum communication based on a silicon chip," Opt. Express **24**, 28731–28738 (2016).
6. D. Pérez-Galacho, C. Alonso-Ramos, F. Mazeas, *et al.*, "Optical pump-rejection filter based on silicon sub-wavelength engineered photonic structures," Opt. Lett. **42**, 1468–1471 (2017).
7. D. Oser, S. Tanzilli, F. Mazeas, *et al.*, "High-quality photonic entanglement out of a stand-alone silicon chip," NPJ Quantum Inf. **6**, 31 (2020).
8. W. Shi, X. Wang, C. Lin, *et al.*, "Silicon photonic grating-assisted, contra-directional couplers," Opt. Express **21**, 3633–3650 (2013).
9. S. Xiao, M. H. Khan, H. Shen, *et al.*, "A highly compact third-order silicon microring add-drop filter with a very large free spectral range, a flat passband and a low delay dispersion," Opt. Express **15**, 14765–14771 (2007).
10. T. Dai, A. Shen, G. Wang, *et al.*, "Bandwidth and wavelength tunable optical passband filter based on silicon multiple microring resonators," Opt. Lett. **41**, 4807–4810 (2016).
11. J. R. Ong, R. Kumar, and S. Mookherjea, "Ultra-high-contrast and tunable-bandwidth filter using cascaded high-order silicon microring filters," IEEE Photonics Technol. Lett. **25**, 1543–1546 (2013).
12. F. Horst, W. M. J. Green, S. Assefa, *et al.*, "Cascaded Mach-Zehnder wavelength filters in silicon photonics for low loss and flat pass-band WDM (de-)multiplexing," Opt. Express **21**, 11652–11658 (2013).
13. J. Lee, W. Lee, M. Kim, *et al.*, "Noise filtering for highly correlated photon pairs from silicon waveguides," J. Lightwave Technol. **37**, 5428–5434 (2019).
14. K. Wang, Y. Wang, X. Guo, *et al.*, "Ultracompact bandwidth-tunable filter based on subwavelength grating-assisted contra-directional couplers," Front. Optoelectron. **14**, 374–380 (2021).
15. J. St-Yves, H. Bahrami, P. Jean, *et al.*, "Widely bandwidth-tunable silicon filter with an unlimited free-spectral range," Opt. Lett. **40**, 5471–5474 (2015).
16. M. T. Boroojerdi, M. Ménard, and A. G. Kirk, "Two-period contra-directional grating assisted coupler," Opt. Express **24**, 22865–22874 (2016).
17. C. S. Hong, J. B. Shellan, A. C. Livanos, *et al.*, "Broad-band grating filters for thin-film optical waveguides," Appl. Phys. Lett. **31**, 276–278 (1977).
18. X. Liang, R. Cheng, X. Shen, *et al.*, "Spectral-distortionless, flat-top, drop-filter based on complementarily-misaligned multimode-waveguide Bragg gratings," J. Lightwave Technol. **38**, 6600–6604 (2020).
19. A. Yariv, "Coupled-mode theory for guided-wave optics," IEEE J. Quantum Electron. **9**, 919–933 (1973).
20. D. Melati, A. Melloni, and F. Morichetti, "Real photonic waveguides: guiding light through imperfections," Adv. Opt. Photonics **6**, 156–224 (2014).
21. D. Charron, J. St-Yves, O. Jafari, *et al.*, "Subwavelength-grating contradirectional couplers for large stopband filters," Opt. Lett. **43**, 895–898 (2018).
22. J. Jiang, H. Qiu, G. Wang, *et al.*, "Broadband tunable filter based on the loop of multimode Bragg grating," Opt. Express **26**, 559–566 (2018).
23. J. Wang, F. Sciarrino, A. Laing, *et al.*, "Integrated photonic quantum technologies," Nat. Photonics **14**, 273–284 (2020).
24. J. W. Silverstone, D. Bonneau, J. L. O'Brien, *et al.*, "Silicon quantum photonics," IEEE J. Quantum Electron. **22**, 390–402 (2016).
25. J. Wang, S. Paesani, Y. Ding, *et al.*, "Multidimensional quantum entanglement with large-scale integrated optics," Science **360**, 285–291 (2018).
26. L. Caspani, C. L. Xiong, B. J. Eggleton, *et al.*, "Integrated sources of photon quantum states based on nonlinear optics," Light Sci. Appl. **6**, e17100 (2017).
27. D. Grassani, S. Azzini, M. Liscidini, *et al.*, "Micrometer-scale integrated silicon source of time-energy entangled photons," Optica **2**, 88–94 (2015).
28. S. Ramelow, A. Farsi, S. Clemmen, *et al.*, "Silicon-nitride platform for narrowband entangled photon generation," arXiv, arXiv:1508.04358 (2015).
29. M. Piekarek, D. Bonneau, S. Miki, *et al.*, "High-extinction ratio integrated photonic filters for silicon quantum photonics," Opt. Lett. **42**, 815–818 (2017).
30. A. D. Simard, G. Beaudin, V. Aimez, *et al.*, "Characterization and reduction of spectral distortions in Silicon-on-Insulator integrated Bragg gratings," Opt. Express **21**, 23145–23159 (2013).
31. C. Qiu, Z. Sheng, H. Li, *et al.*, "Fabrication, characterization and loss analysis of silicon nanowaveguides," J. Lightwave Technol. **32**, 2303–2307 (2014).
32. A. D. Simard, N. Ayotte, Y. Painchaud, *et al.*, "Impact of sidewall roughness on integrated Bragg gratings," J. Lightwave Technol. **29**, 3693–3704 (2011).
33. D. T. H. Tan, K. Ikeda, and Y. Fainman, "Cladding-modulated Bragg gratings in silicon waveguides," Opt. Lett. **34**, 1357–1359 (2009).
34. J. Čtyroký, J. Gonzalo Wangüemert-Pérez, P. Kwiecien, *et al.*, "Design of narrowband Bragg spectral filters in subwavelength grating metamaterial waveguides," Opt. Express **26**, 179–194 (2018).
35. W. Yao, Z. Huang, J. Chen, *et al.*, "Ultralong waveguide grating antenna enabled by evanescent field modulation," Opt. Lett. **47**, 5397–5400 (2022).
36. D. T. Spencer, M. Davenport, S. Srinivasan, *et al.*, "Low kappa, narrow bandwidth Si_3N_4 Bragg gratings," Opt. Express **23**, 30329–30336 (2015).
37. W. Zhang, N. Ehteshami, W. Liu, *et al.*, "Silicon-based on-chip electrically tunable sidewall Bragg grating Fabry–Perot filter," Opt. Lett. **40**, 3153–3156 (2015).
38. D. Pimbi, M. Hasan, M. Borhan Mia, *et al.*, "Polarization-independent photonic Bragg grating filter with cladding asymmetry," Opt. Lett. **48**, 1192–1195 (2023).
39. D. Oser, F. Mazeas, X. Le Roux, *et al.*, "Coherency-broken Bragg filters: overcoming on-chip rejection limitations," Laser Photonics Rev. **13**, 1800226 (2019).
40. S. Zamek, D. T. H. Tan, M. Khajavikhan, *et al.*, "Compact chip-scale filter based on curved waveguide Bragg gratings," Opt. Lett. **35**, 3477–3479 (2010).
41. Z. Zou, L. Zhou, M. Wang, *et al.*, "Tunable spiral Bragg gratings in 60-nm-thick silicon-on-insulator strip waveguides," Opt. Express **24**, 12831–12839 (2016).
42. A. Goswami and B. Krishna Das, "Design and demonstration of an efficient pump rejection filter for silicon photonic applications," Opt. Lett. **47**, 1474–1477 (2022).
43. C. Klitis, G. Cantarella, M. J. Strain, *et al.*, "High-extinction-ratio TE/TM selective Bragg grating filters on silicon-on-insulator," Opt. Lett. **42**, 3040–3043 (2017).
44. D. Oser, D. Pérez-Galacho, X. Le Roux, *et al.*, "Silicon subwavelength modal Bragg grating filters with narrow bandwidth and high optical rejection," Opt. Lett. **45**, 5784–5787 (2020).
45. S. H. Badri and S. G. Farkoush, "Subwavelength grating waveguide filter based on cladding modulation with a phase-change material grating," Appl. Opt. **60**, 2803–2810 (2021).
46. S. H. Badri, S. SaeidNahaei, and J. S. Kim, "Hybrid plasmonic slot waveguide with a metallic grating for on-chip biosensing applications," Appl. Opt. **60**, 7828–7833 (2021).
47. S. Sahu, J. Ali, P. P. Yupapin, *et al.*, "Optical biosensor based on a cladding modulated grating waveguide," Optik **166**, 103–109 (2018).
48. R. Halir, A. Ortega-Moñux, D. Benedikovic, *et al.*, "Subwavelength-grating metamaterial structures for silicon photonic devices," Proc. IEEE **106**, 2144–2157 (2018).